



# Determination of the Forming-Limit Diagram from Deformations within Necking Instability: A Digital Image Correlation-Based Approach

A. Roatta, M. Stout, and J.W. Signorelli

(Submitted December 20, 2019; in revised form March 26, 2020; published online June 26, 2020)

It is now possible using digital-image correlation techniques to precisely measure deformation within a developing necking instability, during forming-limit experiments. However, the current standards for measuring limit strains rely only on data outside of the instability. We propose exactly the opposite, to use just those deformations from the material where the instability will develop. Marciniak and Kuczynski experiments were performed on a drawing-quality steel and the entire deformation history recorded with a high-resolution photographic camera. The strain fields from these image were analyzed with the digital-image correlation program NCORR, concentrating on where the necking instability would form. The Merklein et al. (CIRP Ann Manuf Technol 59:295-298, 2010) and Hotz et al. (Key Eng Mater 549:397-404, 2013) temporal analyses were modified through an original smoothing technique to uniquely identify, through a correspondence of results, when the deformation acceleration rate begins to rapidly increase within the developing instability. This defines a limit strain. These results were compared to the standard Bragard-type determination specified in the norm International Standard ISO 12004-2:2008 (Metallic materials—sheet and strip: determination of forming-limit curves. Part 2—determination of forming-limit curves in the laboratory, International Organization for Standardization, Geneva, 2008). We found a close agreement in balanced-biaxial tension between our proposed technique and the standard Bragard-type analysis. However, in plane-strain and uniaxial deformation the standard analysis appeared to be excessively conservative, by as much as 40% for our steel.

**Keywords** Bragard, correlation coefficient, digital-image correlation, experimental noise, forming-limit diagram, steel

## 1. Introduction

The forming-limit diagram (FLD) is a popular graphical method that quantitatively shows a sheet-metal's ability to deform during forming operations. Keeler and Backofen (Ref 11) and Goodwin (Ref 4) were the first to devise this concept and to demonstrate its utility. Their ideas were based on early biaxial-bulge and plane-strain experiments by Gensamer (Ref 3).

Over the years, the measurement of the FLD has been refined until a norm, ISO 12004-2:2008 (2008) now specifies experimental loading techniques, matrix and punch geometries, and the data analysis procedure. The norm lists two acceptable punch geometries: a semispherical rounded-nose punch (Nakazima et al. Ref 17); and a blunt-nose punch that loads the

sample through a carrier blank that contains a center hole, Marciniak and Kuczynski (Ref 13).

Traditionally, sheet deformation in FLD experiments was measured with circle grids either etched into or deposited on the specimen surface. Deformation would typically fall into three categories: uniform, without any evidence of a plastic-necking instability; deformation including the necking instability; and fracture. Circle measurements gave the deformations associated with these particular phenomena. Different techniques were proposed by various researchers for converting these deformations into an FLD. The practice that has the greatest acceptance today is that based on Bragard et al. (Ref 2), and it is described in the ISO norm. Bragard et al. (Ref 2) proposed examining the measured strain profile across the necking instability. They found that the principle strain normal to the developing instability increased dramatically at the instability and discounted this region from their analysis. They then fitted the remaining data with a polynomial, whose center value was the limit strain. It is clear that how the border is defined between the discounted data and those used for the fitting will dramatically affect the calculated limit strain. This is particularly important for data obtained with the semispherical punch technique as an important strain gradient is present in the principal strain normal to the plastic-necking instability. This gradient is not nearly as strong for the Marciniak and Kuczynski (MK) specimen, which has a planar test section. Currently, the ISO norm specifies the calculation of the second derivative of the strain with respect to position on the sample surface. The maximums in the second derivative define the boundary for discounting or including data points.

A. Roatta and J.W. Signorelli, Instituto de Física Rosario - Consejo Nacional de Investigaciones Científicas y Técnicas, Buenos Aires, Argentina; and Universidad Nacional de Rosario (IFIR-CONICET/UNR), Ocampo y Esmeralda, 2000 Rosario, Santa Fe, Argentina; and M. Stout, Instituto de Física Rosario - Consejo Nacional de Investigaciones Científicas y Técnicas, Buenos Aires, Argentina. Contact e-mail: signorelli@ifir-conicet.gov.ar.

Ghosh and Hecker (Ref 6) and Ghosh (Ref 7) noted many years ago that after the development of a diffuse instability a positive strain rate-sensitive material can continue to sustain deformation within the developing necking instability. For a tensile test the Considéré criterion is well known, which states that the diffuse instability occurs at a strain equal to the Hollomon work hardening exponent:  $\epsilon = n$ . These authors observed that as the strain rate increases due to nonuniform deformation the induced positive strain rate sensitivity stress increase is sufficient to postpone necking until a value of at least  $\epsilon = 2n$  is reached. Ghosh (Ref 7) states that even after the diffuse instability is reached deformation “is quasi stable in nature, it is practically ‘uniform’ and useful,” and he reported that for tensile tests steel can experience nearly 40% of its total elongation after the diffuse instability.

Thus, for positive strain rate-sensitive metals the ISO criterion could be overly conservative, as it relies on the strains outside of the necking instability to determine the material’s limit strains. This could be particularly important in the case of the Marciniak and Kuczynski experiment because there are practically no strain gradients. The deformation outside the instability is at the value of the diffuse instability.

In the past, circle grid measurement, providing only millimeter length-scale resolution, was the only technique available to measure limit-strain deformations. Thus, it was impossible to measure deformations occurring just within a necking instability. Now, the digital-image correlation technique (DIC) gives nearly micron scale resolution for high-quality images and the ability to study the necking instability specifically. Vacher et al. (Ref 19) and Sutton et al. (Ref 18) have applied DIC to measure sheet-metal forming-limit strains. Digital-image correlation gives not only full-field deformation data and much greater resolution than the traditional grid technique, but a temporal history of deformation. For image correlation, a random pattern of fine dark spots is applied over a uniform white background, i.e., a speckle pattern. As deformation of the sample proceeds, successive images of the speckle pattern are recorded, and distortions, expansions and contractions in the pattern give deformations and subsequently strains, through commercial, e.g., GOM (Ref 5) or open-source Blaber et al. (Ref 1) digital-image correlation programs.

A popular method of determining limit strains, based on digital-image correlation data, is to compare strains and strain rates in the area of uniform deformation with those in the necking instability. This takes advantage of the time history and full-field data available from the DIC technique.

In their paper, Martínez-Donaire et al. (Ref 14) examined a profile of points perpendicular to the formed instability for an AA7075-O aluminum alloy. Within the zone that developed into an instability (local neck) the major strain rate increased monotonically with time, whereas outside of it, the strain rate tended to first increase and then decrease. They were able to identify a singular point (time-history curve) on the shoulder of the instability where the major strain rate first increases and then decreases to zero. The time step at which the maximum occurs for this curve defined the limit strain. Wang et al. (Ref 21) compared the through-thickness strain inside and outside of the necked zone and then defined the strain limit in terms of a difference between these two values. Iquilio et al. (Ref 10) used the Marciniak and Kuczynski geometry to measure limit strains. Their results for a 430 stainless steel were based on the time variation of the thickness strain identified at the center and the edge of the necking zone.

Merklein et al. (Ref 15) were some of the first to propose using a statistical method to identify the point at which a plastic flow localization develops in a deforming sheet. While not stated with an explicit equation in their paper, they proposed using a correlation coefficient to determine when the time history of the second derivative of the major plastic strain deviates from linearity. Their analysis has the advantage that it can be applied to only the deformations within the necking instability. Analyzing experimental data, they showed a peak in the correlation coefficient that is associated with a rapid rise in the strain-acceleration/time curve—the development of the necking instability. And finally, they took the strains from the image associated with this peak as the limit strains.

The work of Merklein et al. (Ref 15) was expanded upon by Hotz et al. (Ref 8). They proposed adding a linear function to the strain-acceleration data and passing a band with a finite number of points, for example seven points, through these data. The correlation coefficient for the point in the center of the band is calculated using just those data within the band. In essence, this gliding analysis examines the curvature of the strain-acceleration versus time/image number curve. Contrarily, Merklein et al.’s technique sums all the data up to the point for which the correlation coefficient is being calculated. In addition, Hotz et al. examined the “linear best fit method” that uses the first time-based derivative of the thinning rate, proposed by Volk and Hora (Ref 20).

Recently, Min et al. (Ref 16) examined a number of time-dependent methods for several materials, including two high-strength steels (DP600 and MP980) and an aluminum alloy (AA6022-T4). Some of the techniques they studied over-predicted limit strains, and some appeared to give excessively conservative values. The techniques of Hotz et al. (Ref 8) were intermediate in their findings.

Despite these studies, an accepted technique to define a material’s limit strain based on the deformation within the necking instability has not emerged, and the community continues to rely on the Bragard-type analysis. Many of the temporal techniques compare deformation outside of the instability to that within. They thus suffer from uncertainties of geometry and how the instability profile might change for particular strain paths. In addition, it is necessary to calibrate the comparison of deformations and that has routinely been done to match results from the standard Bragard-type analysis. Other analyses have been based on achieving a strain rate of zero outside of the instability. From our experiments on steel, even as the material fails the strain rate outside of the instability never drops to zero. The analysis proposed by Merklein et al. (Ref 15) is one of the most promising. It can be based on only the deformation within the necking instability and is purely mathematical in nature, removing investigator interpretations and prejudices. However, from our experience, it is inconsistent from experiment to experiment, producing inconsistent results between experiments and over different strain paths. We have had better results applying the gliding correlation coefficient analysis of Hotz et al. (Ref 8), but experimental noise in the calculated gliding correlation coefficient has cast uncertainty in the exact location of the maximum curvature in the strain-acceleration curve.

To date most all the research using digital-image correlation to measure limit strains has focused on developing a particular new technique for using temporal strain-field data for determining a limit strain. The equivalencies in the early days of metal forming were the discussions on how to specify which

circles in the grid pattern had experienced post uniform deformation and which had not, or whether to use actual deformations to determine the limit between safe and unsafe forming strains or the maximum of a curve fitted to the deformation gradients away from the necking instability, the Bragard approach. Considering that Bragard et al.'s original paper was published in 1972 and it was not until 2008, 36 years later, that this criterion was specified in an ISO norm, it is not surprising that no accepted digital-image correlation, temporal analysis has yet emerged.

What is unique and novel about this work is that we are not attempting to develop a completely new analysis, but rather we are seeking to understand the differences of what happens outside and inside of a necking instability and how the measurement of these differences, if there are any, might lead to a more accurate forming-limit diagram.

Because the techniques of Merklein et al. and Hotz et al. can examine only the deformation within the developing necking instability and are purely mathematical in nature we believed they were the most promising. We thus first undertook a theoretical study to determine why results were inconsistent and to see how the DIC data could be treated to yield unique and consistent limit strains from the correlation coefficients. Such limit strains would generate a FLD based on solely the deformation within the zone that would become the necking instability, thus providing a complement to the standard Bragard-type analysis.

## 2. Theoretical Considerations

The techniques of Merklein et al. (Ref 15) and Hotz et al. (Ref 8) employ only the strain fields measured by digital-image correlation and the time or image number. Both of these quantities are known unequivocally. In addition, if the identical procedure is used to analyze each limit-strain experiment, variabilities due to sample geometry, instability profile and specimen strain path should be minimized.

Pearson's correlation coefficient,  $r$ , seeks a linear relationship between two variables  $x$  and  $y$ :

$$r = \frac{\sum_i (x_i - \bar{x})(y_i - \bar{y})}{\sqrt{\sum_i (x_i - \bar{x})^2} \sqrt{\sum_i (y_i - \bar{y})^2}} \quad (\text{Eq 1})$$

whereas is usual,  $\bar{x}$  and  $\bar{y}$  are the means of the variables  $x_i$  and  $y_i$ , respectively. The sum runs from  $i = 1$  to  $N$  where  $N$  is the number of pairs of the quantities  $(x_i, y_i)$ .

Taking two points that define a nonhorizontal, perfect line, clearly shows  $r = 1$  for a line with a positive slope and  $r = -1$  for a negative slope. If the line is horizontal the coefficient  $r$  is undefined, while in the case of a perfectly random or ordered group of data that has no linear tendency, the coefficient  $r$  is zero. The random noise associated with experimental data provides such a characteristic. In Merklein et al.'s (Ref 15) and Hotz et al.'s (Ref 8) analyses, the importance and effects of experimental noise in the displacement measurements through image correlation are greatly amplified by taking three derivatives before calculating Pearson's coefficient. The first derivative of displacement gives strain, the next strain rate and the final strain acceleration.

When working with a limited number of perfect points, it is easy to see how Pearson's equation functions. It is not nearly as

clear for a collection of data, which contain inevitable experimental scatter. This warrants a theoretical study using known analytic functions to model an actual experiment.

### 2.1 Modeling Strain Versus Time/Image Number Data

If the experimental strain versus time (image number) curve is modeled with a mathematical function, the effects of experimental noise can be eliminated from the calculation of Pearson's coefficient. We selected the strain/time curve from a plane-strain Marciniak and Kuczynski limit-strain experiment and defined our function(s) to fit these data. It should be noted that the experimental data consisted of a strain history from 150 points equally spaced in time and terminating with the final image before fracture appeared. The complete strain/time curve, up to and through image 150, was fitted with a double exponential:

$$\varepsilon_1|_{t=1 \text{ to } 150} = \varepsilon_0 + A_1 e^{\frac{(t-t_0)}{c_1}} + A_2 e^{\frac{(t-t_0)}{c_2}} \quad (\text{Eq 2})$$

where  $t$  is time or image number,  $\varepsilon_1$  is the strain at time  $t$ , and  $\varepsilon_0$ ,  $t_0$ ,  $A_1$ ,  $A_2$ ,  $c_1$ , and  $c_2$  are constants, which are listed in the Appendix—Part I Constants.

The work of Hotz et al. (Ref 8) demonstrated that once an instability forms the strain acceleration within the instability increases rapidly and again establishes a nearly linear relation with time. Thus, the correlation coefficient of Hotz et al.'s (Ref 8) gliding band rises, to again approach a value of one. The double-exponential description of strain/time never obtains such linearity in strain acceleration after the instability forms. Because of this, we replaced the double-exponential fit to the strain data after the beginning of the instability, images 140 to 150, with a third-order polynomial:

$$\varepsilon_2|_{t=140 \text{ to } 150} = a(t-140)^3 + b(t-140)^2 + c(t-140) + \varepsilon_1|_{t=140} \quad (\text{Eq 3})$$

where  $a$ ,  $b$  and  $c$  are constants listed in the Appendix—Part I Constants. The parameters  $a$ ,  $b$  and  $c$  are related to the first, second and third derivatives of the double-exponential function at a time of 140. Thus, the slopes of the two functions for strain, strain rate and strain acceleration were spliced seamlessly.

### 2.2 Application of Pearson's Coefficient to the Analytic Functions

Four curves are plotted in Fig. 1. Figure 1(a) shows strain versus image/time. The experimental strain data obtained from the forming-limit test are plotted versus image number/time. Colored curves from the two analytic functions lie in turn over these data. One can see that the analytic functions merge seamlessly and give an accurate description of the experiment. It is important to remember that the two functions represent a case of *zero* experimental noise.

The first and second derivatives of the strain/time functions are plotted in Fig. 1(b) and (c). It is apparent that the elbow in the curves, indicative of a deformation instability, sharpens with each derivative. No discontinuities appear where the functions were merged. A second curve appears in Fig. 1(c) that applies to the analysis of Hotz et al. (Ref 8). In this case, a linear function passing through zero with a slope of  $5 \times 10^{-5}$  was added to the strain acceleration.

We have plotted the correlation coefficients in Fig. 1(d), for the two strain-acceleration curves in Fig. 1(c). It must be

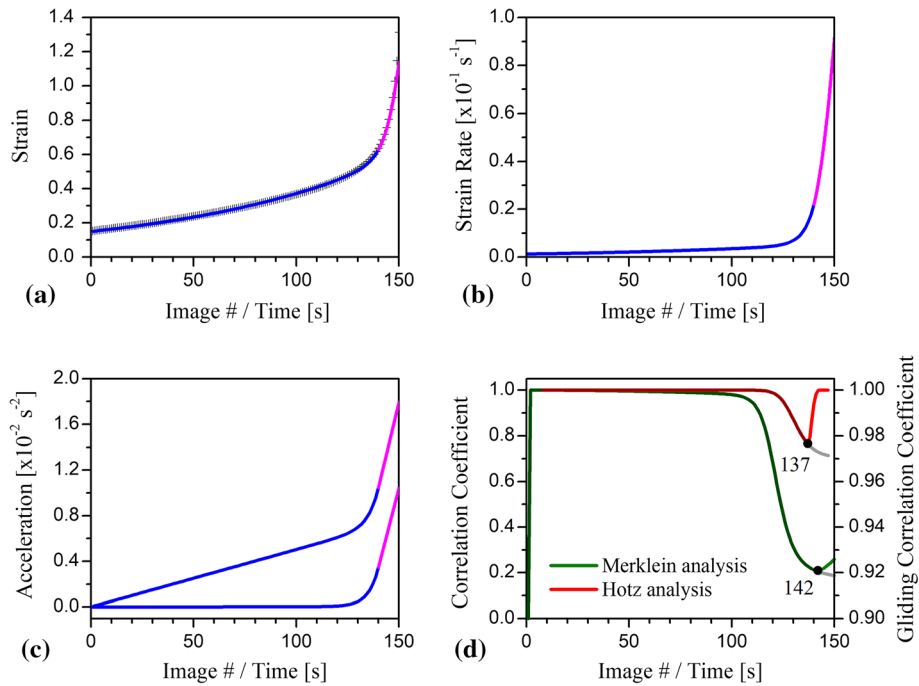


**Fig. 1** Double-exponential and third-order polynomial curves: (a) strain, (b) strain rate, (c) strain acceleration and strain acceleration summed with a linear function and (d) correlation coefficients based on the analyses of Merklein et al. (Ref 15) and Hotz et al. (Ref 8). The gliding and full correlation coefficients are shown for both the double-exponential and third-power polynomial and simple double-exponential functions

remembered that the two curves result from different applications of Pearson's correlation coefficient. In the case of Merklein et al.'s (Ref 15) analysis all of the data is summed up to the data point where the correlation coefficient is calculated. For Hotz et al.'s (Ref 8) analysis a band of a fixed number of points is passed over the data. Only the data within the gliding band are used to calculate the correlation coefficient for the data point at the center of the band. In the case of our analysis with a total of 150 images, we selected a band width of seven points.

For the double-exponential and third-power polynomial function, the correlation coefficient has a value of one as the band glides over the points dominated by the linear function. The coefficient dips into a valley that bottoms at a value just below 0.98 for image 137—the point of maximum curvature in the strain acceleration—and then rises again with the linearity of the rapidly increasing strain acceleration. This acceleration would be from deformation within an actual necking instability in the case of an experimental limit-strain test. This ideal behavior matches that seen in experiments reported by Hotz et al. (Ref 8).

Figure 1(d) also shows the gliding correlation coefficient curve calculated for only the double-exponential function, the light gray curve. One sees that as the strain-acceleration elbow is reached, this curve drops but then continues to decrease and never recovers to one as it does for Hotz et al.'s (Ref 8) data and the double-exponential and third-power polynomial function.

In the case of Merklein et al.'s (Ref 15) analysis, the ideal function also begins with a correlation coefficient of  $r = 1$ . As deformation proceeds,  $r$  begins to slowly decrease, from the curvature of the double exponential and then falls rapidly as the plastic instability develops. Again, both the spliced and simple double-exponential correlation coefficient curves are shown. They are equivalent to time/image number 142 and then begin

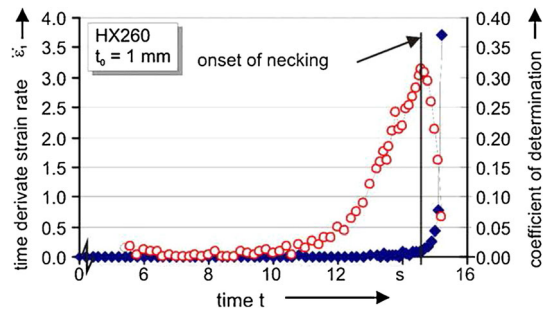


**Fig. 2** The results presented by Merklein et al. (Ref 15) in their original paper. Reprinted from CIRP Annals—Manufacturing Technology, Vol 59, Ed 1, M. Merklein, A. Kuppert, M. Geiger, Time dependent determination of forming limit diagrams, pp 295–298, Copyright 2010, with permission of Elsevier

to diverge. The simple double-exponential curve, light gray, continues to drop from point 142, while the correlation coefficient of the spliced double-exponential, third-power polynomial curve begins to increase slightly. We attribute this slight rise to the perfect linearity of the second derivative of the third-power polynomial.

The form of either curve is *completely different* from that documented in Merklein et al. (Ref 15), for actual experimental data (Fig. 2).

Merklein et al. (Ref 15) show both the strain acceleration (time derivative of strain rate) and the correlation coefficient (coefficient of determination) in their figure. The correlation coefficient advances from a zone of uniform deformation with a value of nearly zero. The curve then begins to rise, encounters a maximum and falls. Merklein et al. take the strain associated with the maximum as the limit strain.



The notable difference between our functional model and Merklein et al. (Ref 15) is that our functions are perfectly smooth, while Merklein et al. (Ref 15) report data from an actual experiment. As with any experiment, these data inevitably exhibit a degree of experimental noise. There is a precision involved in any displacement measurement including that by digital-image correlation, and after that measurement, three derivatives are taken to obtain the strain acceleration. This greatly amplifies any slight noise that might be present in the initial measurement.

How might noise affect our perfect analytic functions and the two correlation coefficient analyses?

### 2.3 The Addition of Noise to the Functional Correlation Coefficient Analyses

The strain, Fig. 1(a), ranged between 0.15 and 1.4. In order to approximate experimental noise, a random value was added to each individual data point. This value was taken from a Gaussian distribution centered at zero with a standard deviation of 0.01 and scaled by the factor 0.001. The time/image numbers, from 1 to 150, were left exact and unchanged.

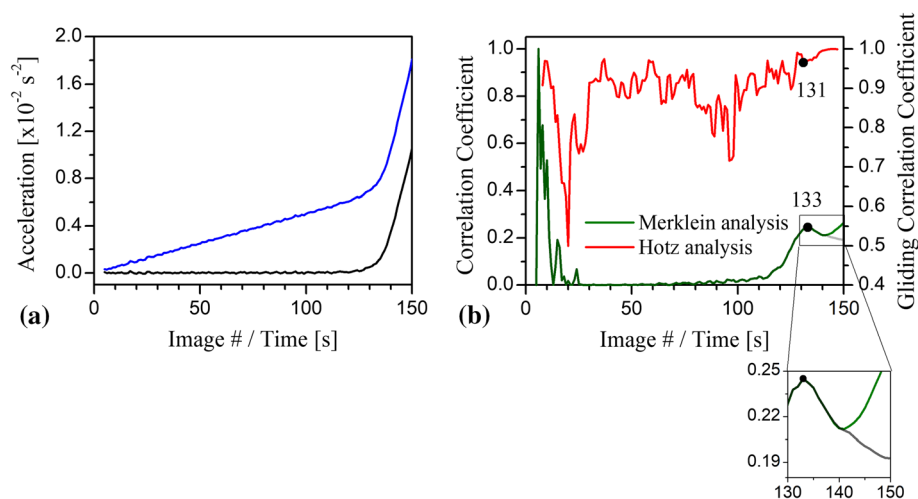
A practical method to smooth experimental data is to define a band of experimental points, much like in the Hotz et al. (Ref 8) analysis, and to fit a polynomial to this band. The value of the polynomial at the central point becomes the experimental value of this point. If a fourth-order polynomial is used, it can be easily differentiated to obtain acceleration, also at the bands central point. The band is then passed over the complete data set. It should be noted that for a fourth-order polynomial a minimum band width of five points is needed. In this theoretical analysis, we adopted this technique to examine how different amounts of noise and smoothing, imposed on the perfect functions, would affect the correlation coefficients. Thus, the results of the theoretical analysis can be applied directly to actual data.

Figure 3(a) and (b) shows the strain-acceleration and its Pearson correlation coefficient curves after the addition of the scaled, random noise and polynomial smoothing. Nine points were used in the polynomial smoothing. Again, for Hotz's analysis, a linear function with a slope of  $5 \times 10^{-5}$  was summed with the standard strain-acceleration curve. Now, a

slight waviness from the random noise appears in the strain-acceleration curves, see Fig. 3(a). The effect of this slight noise on the correlation coefficients is dramatic. The correlation coefficient curve in Fig. 3(b) now has the form shown in Merklein et al. (Ref 15). The curve rapidly descends from one (two data points) to zero and tracks there until the time/image number of about 110. The curve then rises to a maximum of  $r = 0.245$  at image 133. After this, it descends again. Two curves are shown after the maximum at time/image number 133: the heavy green for the spliced double-exponential, third-power polynomial function; and the light gray for the simple double exponential. Here, as shown in Fig. 1(d), the simple double-exponential curve continues to decrease, while for the spliced double-exponential and third-order polynomial curve there is an upward tail. As stated earlier, we believe this tail is a result of the perfect linearity of the second derivative of the third-order polynomial, and we regard it as an artifact of the spliced function, which should be discounted.

Interpreting Hotz et al.'s (Ref 8) gliding correlation coefficient is much more difficult. The effect of the imposed noise begins from the first images and exhibits peaks and valleys between correlation coefficients of 0.5 to 0.95, over the full data range. There would be no way to identify the maximum of curvature based solely on a minimum of  $r$ . If we look at the gliding strain-acceleration data, it appears that the maximum in curvature corresponds to the final valley in the gliding correlation coefficient. The full correlation coefficient has a maximum that corresponds to this final valley, as well. But, identifying a limit strain based only on these two criteria is neither rigorous nor satisfying.

Figure 4(a) and (b) shows the same calculations but for a polynomial smoothing with 11 points, which further reduces the noise we have imposed on the double-exponential and third-power functions. There are still peaks and valleys in the gliding correlation coefficient, but they are much reduced, between one and 0.90 up to the point of maximum curvature. Here,  $r$  has a value of 0.96, pointing to the elbow in the strain acceleration. After the point of maximum curvature, the gliding correlation coefficient again rises to one. The minimum in  $r$  occurs at image 132. Considering these results for greater smoothing confirms that the maximum curvature in strain



**Fig. 3** Strain accelerations and correlation coefficients for the full and gliding analyses after the addition of random noise and smoothing with a polynomial fitted to nine points: (a) accelerations; (b) correlation coefficients

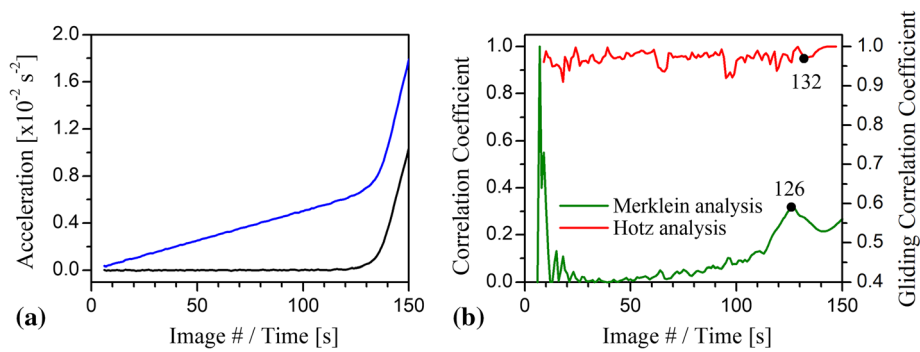


**Fig. 4** Strain accelerations and correlation coefficients for the full and gliding analyses after the addition of random noise and smoothing with a polynomial fitted to 11 points: (a) strain accelerations; (b) correlation coefficients

acceleration for the gliding correlation coefficient indeed coincides with the final valley in Fig. 3(b).

There is also a clear peak in the full correlation coefficient, which is higher than for the less smoothed data and shifted to smaller deformations. For the 11-point polynomial smoothing, the peak is at image 126. Other analysis with different numbers of smoothing points confirmed that the peak in the full correlation coefficient moves to the left, a lower strain limit, as the smoothing increases. Less smoothing causes the peak to shift to higher limit-strain values.

Clearly, the limit strain predicted by Merklein et al.'s (Ref 15) correlation coefficient analysis is very dependent on experimental noise, and it is not unreasonable to expect that this noise might vary between experiments along different strain paths or even between experiments covering the same strain path. This would in turn produce the inconsistencies observed in the limit-strain results. Hotz et al.'s (Ref 8) gliding correlation coefficient result is practically independent of noise and it is defined by a completely separate phenomenon in the strain-acceleration/time curve from the Merklein analysis. Figure 3 and 4 demonstrate that by varying the amount that data are smoothed, here a theoretical and thus ideal data set, coincidence between the two techniques can be obtained. The image where such coincidence is obtained would define a unique limit strain that is consistent between experiments. Thus, by smoothing actual experimental data we can also obtain a correspondence between the Merklein and Hotz techniques. A limit strain obtained in this manner would be unique and consistent between experiments and over different strain paths, which is not now the case. And, such a limit strain would be from that data taken directly from within the zone of the necking instability. We performed an experimental FLD determination for a cold-rolled steel in this way and with the Bragard-type technique to directly compare limit-strain determinations inside and outside of the necking instability.

### 3. Experimental Technique, Material and Analysis

We elected to use a scaled version of the MK sample geometry, the digital-image correlation program Ncorr, Blaber et al. (Ref 1), and a cold-rolled steel for the forming-limit measurements. After the tests were conducted, both the Bragard-based analysis ISO 12004-2:2008 (2008) (Ref 9) and the statistically based, smoothed variation of the temporal

Merklein et al. (Ref 15) and Hotz et al. (Ref 8) techniques were used to analyze the experimental results.

#### 3.1 Experimental Equipment and Technique

The MK experiment has a test section with a planar geometry and no through-thickness stress. Thus, during a forming-limit-strain experiment, temporal surface-strain data can be recorded with only a single camera and analyzed using a 2-D digital-image correlation program. These characteristics led to the design of a planar punch, die and camera support system that could be mounted in a universal testing machine, for conducting scaled MK laboratory tests, see Leonard et al. (Ref 12). Using the equipment, sample geometries and testing techniques described in that work, we conducted MK limit-strain experiments for a cold-rolled steel over the full range of the forming-limit diagram, from uniaxial tension through plane strain to balanced-biaxial tension.

In this design, the camera support is mounted to the test punch and descends with it during the test. In this way, the distance between the sample and camera, focus and magnification is maintained during the experiment.

High-resolution images were recorded with a commercial photographic camera, Nikon D3300, which had a 4500 × 3000 pixel CCD. This camera allowed us to photograph the developing instability with greater resolution than would be afforded with a high-speed video camera. This was important because the correlation coefficient analyses of Merklein et al. (Ref 15) and Hotz et al. (Ref 8) use only the parts of the image within the necking instability. The Bragard-type analysis on the other hand takes advantage of the full deformation field outside the formed instability. An AF-S DX Micro NIKKOR 85-mm equivalent lens allowed the camera to be focused over the short distances associated with this experiment and filled the CCD recording frame with the ~ 30 mm diameter planar specimen surface.

We conducted the MK experiments at a punch velocity of 1.5 mm/min, which resulted in a typical strain rate at the time of necking between  $5 \times 10^{-3}$  and  $5 \times 10^{-2}$  s<sup>-1</sup>. While this strain rate is low for forming process, it is typical of plasticity experiments. The lower rate afforded an isothermal experiment with better control. This allowed us to pause the experiment at half the limit strain to heat treat the carrier blank, which was from the same steel sheet as the test specimens. Thus, cracking in the blank's center hole was avoided for all experiments. The direction of the major strain was set to be perpendicular to the

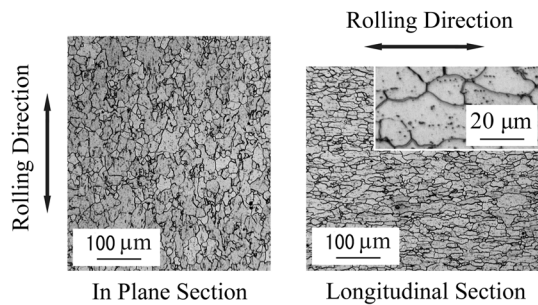


**Fig. 5** Optical micrographs of the steel's microstructure in the in-plane and longitudinal sections. The rolling direction is indicated for these sections. A high-magnification micrograph has been inset on the longitudinal section to show the carbide stringers

rolling direction of the sheet, as suggested in the ISO norm (2008).

### 3.2 Material Properties

A common material typically formed using drawing or stretching processes is advantageous for a basic study of data analysis techniques. Thus, a cold-rolled, steel sheet was selected. Although the supplier did not specify the steel's grade, A1008—0.10% C—is a standard specification for this material. The steel sheet was 0.9 mm thick, sufficiently thin to avoid bending or through-thickness strain gradients, for the reduced-scale experiments.

The in-plane and longitudinal section microstructures of the steel are shown in Fig. 5. The steel had a grain size between 30 and 15  $\mu\text{m}$ . The grains were slightly pancaked in plane and elongated in the rolling direction. Very fine carbide stringers were also present and aligned with the rolling direction. These stringers are shown running horizontally across the grains in a high-magnification inset on the longitudinal section micrograph.

The steel's engineering mechanical properties are listed in Table 1. The sheet has nearly equal yield, hardening and ultimate tensile strengths at 0°, 45° and 90°, as well as approximately equivalent total elongations, between 35 and 38%. These properties are typical of drawing-quality steels with the exception of the yield strength, which at 200 MPa is a bit below what is considered common. The  $R$  values or Lankford coefficients (plastic anisotropy coefficients) measured at 15% strain were 1.75, 1.30 and 2.05 for 0°, 45° and 90°, respectively, to the rolling direction. These values are again typical of a drawing-quality steel. As with other steels, this sheet was positive strain rate sensitive. In its standard form, the strain rate sensitivity exponent  $m$  is expressed as:

$$\frac{\sigma_2}{\sigma_1} = \left( \frac{\dot{\epsilon}_2}{\dot{\epsilon}_1} \right)^m, \quad m = \frac{\ln(\sigma_2/\sigma_1)}{\ln(\dot{\epsilon}_2/\dot{\epsilon}_1)} \quad (\text{Eq 4})$$

where for our steel,  $m = 0.015$ . This result was taken at room temperature for strain rate jumps between  $10^{-4}$ ,  $10^{-3}$  and  $10^{-2}$   $\text{s}^{-1}$ .

### 3.3 Digital-Image Correlation Analysis

The open-source 2-D digital-image correlation program Ncorr, Blaber et al. (Ref 1), was used to calculate the strain-field histories for our MK forming-limit experiments. Ncorr is a MATLAB program with an intuitive graphic user interface. We

selected parameters within Ncorr to precisely resolve strains within an actual deformation instability: subset radius = 50 pixels; subset spacing = 2 pixels; diff. norm cutoff =  $10^{-6}$ ; and number of iterations cutoff = 50. A digital-image correlation program measures displacement and then performs what is in essence a differentiation to calculate strain. Ncorr takes a region containing a finite number of data points to obtain the strains at a central point. If the region specified contains too many points, fidelity at the instability is lost. Taking too few points might result in excessive noise and numeric artifacts. We used a radius of 5 points, 81 data points in total, for the Ncorr strain calculation. In the Appendix—Part II Strain Radius, we show that this number of points did not result in a loss of fidelity at the plastic instability. As mentioned previously, this analysis was applied to  $4500 \times 3000$  pixel CCD images with the deforming part of the MK specimen occupying nearly the entirety of the camera's full field of view.

Using aerosol cans, a speckle pattern of fine, random, black spots was applied over a white background covering the MK specimen surface. We used a slow drying (1 h before applying a second coat) paint for both the background and spots. Thus, the paint remained viscous throughout the experiment, and it could support the very high deformations occurring within the deformation instability, as the limit strain was approached.

### 3.4 Bragard and Merklein/Hotz Analyses

We based our Bragard analysis on the procedure detailed in the ISO 12004-2:2008 norm (Ref 9). The norm states that the final image before fracture is used for the calculation. Obviously in this image, the strain within the deformation instability is very high. The width of this region is defined by the maximums of the second spatial derivative of the major strain profile across the full specimen surface. The central region bounded by the maximums is discarded, and the two regions remaining are fitted with an inverse, second-order polynomial function. The value of the polynomial at the center of the discarded region is taken as the major limit strain. Determining the minor limit strain is a three-step process. Firstly, constancy of volume is used to calculate the through-thickness strain, from the digital-image correlation results ( $\epsilon_{xx}$ ,  $\epsilon_{yy}$ ). Secondly, the central region is again discarded and an inverse polynomial again fitted to the remaining parts of the through-thickness strain profile. Finally, from the central point of the fit, constancy of volume is used to back calculate the minor limit strain.

An advantage of the MK sample is that the strain profiles outside of the deformation instability are very flat. Thus, the outer limits selected for the fit had very little effect on the limit-strain results. In the cases of deformation states between plane strain and uniaxial tension, there was a small gradient between the outer limits of the specimen and the discarded central zone. In these cases, we selected an outer limit of the fitted points in order to maintain coincidence between the fitted points and the arc of the inverse, second-degree polynomial, see Fig. 6(b).

In the case of the Bragard analysis, experimental noise does not seriously affect the limit-strain results. However, as we have seen, noise and its magnitude are very important for the correlation coefficient analysis of Merklein et al. (Ref 15). To adjust the amount of noise present, as was done for the theoretical analysis, we fitted a fourth-order polynomial to the experimental strain/time data. Obviously, a single fourth-order polynomial will not accurately describe the entire strain/time



**Table 1 Mechanical properties of the steel used in this study**

Orientation wrt. the rolling direction, °	0.2% offset yield strength, MPa	Ultimate tensile strength, MPa	Total elongation	Lankford coefficient
0	200	319	0.384	1.75
45	200	342	0.357	1.30
90	200	319	0.350	2.05

Quantities are given in terms of engineering stress and strain

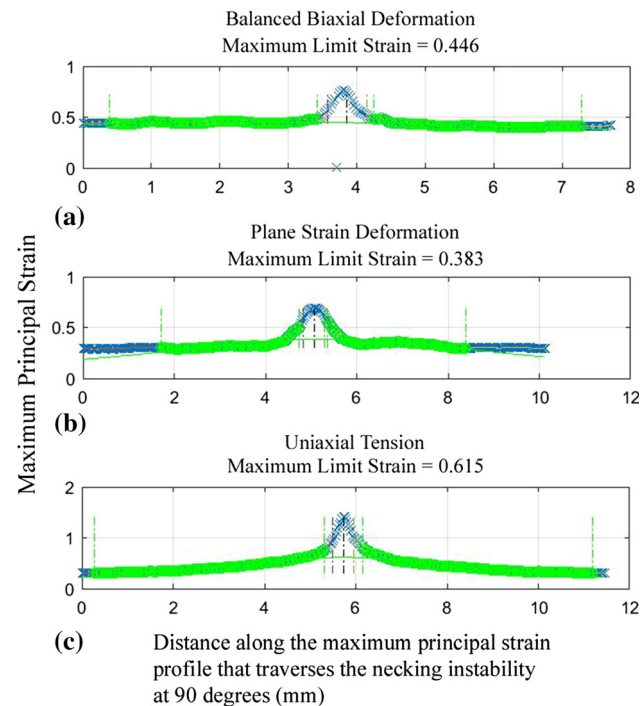


**Fig. 6** Profiles of true, logarithmic, maximum principal strain for (a) balanced-biaxial, (b) plane strain and (c) uniaxial tension deformation are shown. The points fitted with an inverse polynomial to determine the limit strain are highlighted, and the limit-strain values for these profiles are noted

(image number) curve. Thus, a band with a finite odd number of points was passed over the data. The minimum number of points the band can contain is five, and the maximum is only limited by the number of images. From the fit, the value of strain and its two time derivatives are known at the central point of the band. The initial data points of the strain/time data are not the most important, as they happen well before the instability occurs. Thus, if for example a band of eleven points was considered, we would begin evaluating the polynomial for data point six, using five points before and five after. In the case of the final strain values, data cannot be dismissed, as these strains coincide with the deformation instability. In these cases, the fitting was done using the coefficients of the final polynomial calculated for all 11 points and the actual image number/time of the final five points.

As discussed by Merklein et al., data from only a single-pixel point of the digital-image correlation analysis are not reliable. They assumed a circular region of points centered at the point of maximum major strain (within the necking instability) and took an average of this complete data set for

each image. Their correlation coefficient is then calculated from the strain/time history of this group of points. Clearly, the value of the circle's radius that is selected will change the results. The bigger the radius selected the more points away from the center of the instability, with smaller strains, that will be included in the analysis.

The appropriate radius of points taken might change from experiment to experiment and from strain path to strain path, depending on the width and geometry of the deformation instability. The ISO 12004-2:2008 (Ref 9) analysis uses the maximums of the second derivative of strain versus distance (i.e., the spatial derivative) to define a zone of excluded points, points within the necking instability. We took half the width of this zone as the Merklein radius. Thus, our Bragard-type analysis was based only on data outside of the necking instability and our temporal Merklein/Hotz correlation coefficient analysis relied exclusively on data within the plastic instability.

Finally, we should state again that our temporal analysis is based on Pearson's correlation coefficient, Eq 1. This coefficient seeks a linear relationship between two variables, in this case the second derivative, acceleration, of strain versus image number or time. The analysis of Merklein et al. (Ref 15) sums all points up to the point of interest, while the analysis of Hotz et al. (Ref 8) calculates the correlation coefficient for a band of points—typically five, seven or 11 points—that passes through the data. Thus, Merklein et al. define a limit strain based on the deviation from linearity in the strain-acceleration/time curve as the necking instability forms. The analysis of Hotz et al. seeks a maximum in curvature in the same strain-acceleration curve, to which a linear function has been added.

## 4. Experimental Results

Both the Bragard and time-history methods of determining limit strains were used in evaluating the MK forming-limit experiments. The Bragard analysis, ISO (2008), has the advantage that it has been transformed into an accepted norm and thus serves as a reference for both the Merklein et al. (Ref 15) full correlation coefficient, and Hotz et al. (Ref 8) gliding correlation coefficient analyses.

### 4.1 Bragard-Type Analysis

In Fig. 6, we show a true or logarithmic maximum principal strain profile for three strain paths: balanced-biaxial tension; plane-strain deformation; and uniaxial tension. The strain measurement was taken from the final image before fracture appeared. Thus, the plastic flow instability was fully developed.



The highlighted points were used for fitting the inverse second-order polynomial from which the limit-strain values were taken. The peak in the center of the profile results from the necking instability, and one can clearly see the inner limits of the fitting window obtained from the maximums of the second derivative of strain with respect to distance. The points within these limits were discounted.

Outer limits of the fitting were selected to maintain a smooth arc through the data in the fitted polynomial. It is notable that the strain profiles are remarkably flat for all of the strain paths and the outer fitting limit had little effect on the limit-strain results.

The flat strain profiles are a distinct advantage of the MK sample geometry. It was only in the case of the plane-strain results that the outer fitting limits were shortened to maintain the inverse polynomial's arc.

Only a single strain profile is shown in Fig. 6, for each strain state, but as suggested by the ISO standard, ISO (2008), an average of results from five parallel strain profiles was taken from each experiment to determine that experiment's limit strain. It should be noted that the MK specimen strains were very uniform, and there was very little variation in the results that were averaged from the five profiles.

#### 4.2 Temporal Analysis

Figure 7 shows our results for the standard Pearson's and gliding correlation coefficient analyses for the plane-strain specimen whose Bragard profile is plotted in Fig. 6(b). We smoothed the strain/time (image number) data with a gliding fourth-order polynomial as discussed. In this case, five and 11

points were used to determine the polynomial's value at each point in the time history (for each image). In the case of the Hotz analysis, we have indicated on the strain-acceleration curves the bounds of the gliding band at the point of maximum curvature. For the Merklein analysis the location of the peak in the correlation coefficient is shown on the strain-acceleration data.

Examining the acceleration curves, the reduction in noise with additional smoothing points is clear. We selected seven points for the calculation of the gliding correlation coefficient. It can be seen in Fig. 7(a) and (c) that the positions of the band's end points are relatively consistent for the different amounts of smoothing. The curvature maximums are centered at time/image number 147 and 144 for a polynomial smoothing with five and 11 points, respectively.

As seen in the theoretical analysis, contrary to the point of maximum curvature, the gliding correlation-coefficient values are extremely sensitive to noise in the strain/time (image number) data, Fig. 7(b). When we smoothed the strain/time data with only five points, the minimum number possible, values of this correlation coefficient covered the full spectrum, from one to zero. Based on these data alone we would not have been able to identify the gliding correlation coefficient associated with the maximum curvature. This minimum was clear when the data were smoothed using 11 points, Fig. 7(d).

The location of the peak value of the full correlation coefficient, the criterion used by Merklein et al. (Ref 15) to identify the limit strain, was also very sensitive to smoothing. Smoothing with 11 points resulted in a peak at image 134, while the peak occurred for image 148 when smoothing with

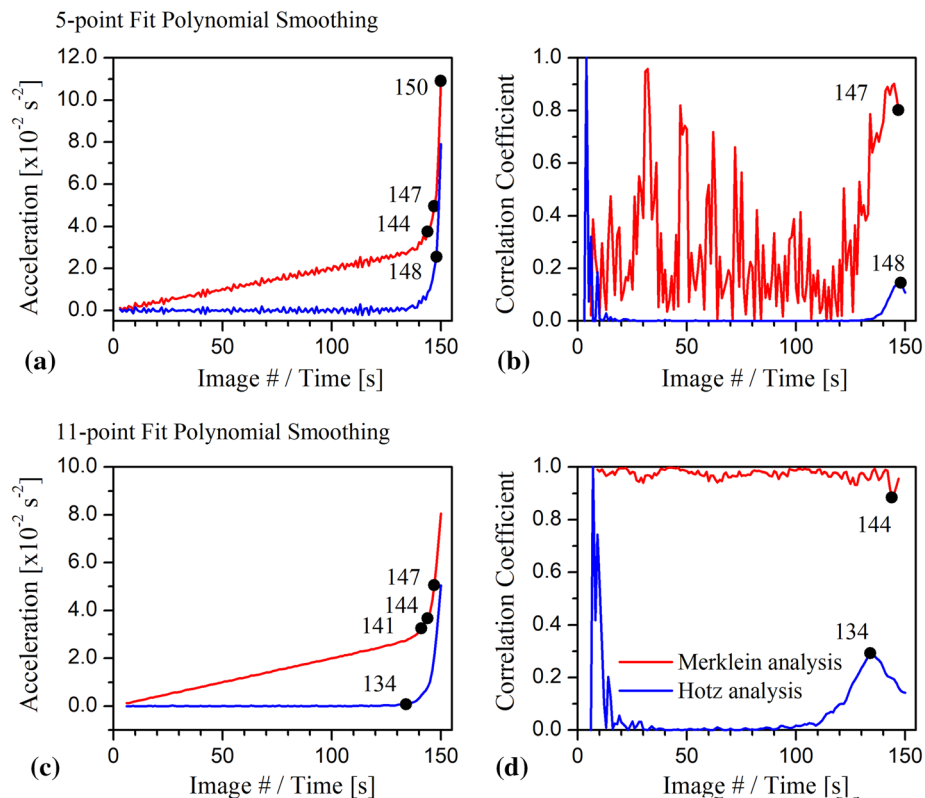


**Fig. 7** The Merklein et al. (Ref 15) and Hotz et al. (Ref 8) correlation coefficient techniques applied to a plane-strain MK sample. We show the strain-acceleration curves (a) and (c) as well as the correlation coefficient plots, (b) and (d). The experimental strain/time data were smoothed with a five- and 11-point fourth-order polynomial

five points, Fig. 7(b) and (d). This difference would give a dramatic difference in measured limit-strain values. Hotz et al. (Ref 8) refer to the full correlation coefficient analysis as “unstable,” but they do not specify exactly what they mean with this terminology. It is perhaps this sensitivity to experimental noise.

In our analysis following Merklein et al., if one looks at where the time/image number point associated with the correlation coefficient peak lies on the strain-acceleration curves, one sees that it too is very sensitive to the amount of smoothing, Fig. 7(a) and (c). When 11 points were used for smoothing, the limit-strain image occurs where the strain-acceleration curve is still nearly linear, before the elbow in this curve associated with a developing instability. The limit strain predicted from this image would appear to be excessively conservative. When smoothing is with five points, Fig. 7(a), the limit-strain image is well up the elbow of the strain-acceleration curve, but still several images before fracture occurs. Obtaining limit strains from this image would seemingly give a more appropriate result.

In their paper, Hotz et al. (Ref 8) state that their gliding correlation coefficient underestimates the limit strain, while the analysis of Merklein et al. (Ref 15) overpredicts this value. They show in a qualitative figure that when the two analyses correspond the limit-strain value is appropriate. For the example shown in Fig. 7, this would occur for a smoothing with five points. In this case, the Hotz gliding correlation coefficient minimum would be for image 147 and the Merklein full correlation coefficient peak is at image 148. If we take the circle-averaged principal strains from image 147, we find a true maximum limit strain of 0.527. This is a limit-strain value for within the instability, and it compares to the average Bragard-determined maximum true limit strain of 0.373, obtained from the diffuse instability strains outside of the necking instability.

#### 4.3 Strain Fields

The strain-acceleration and correlation coefficient curves shown in Fig. 7 are some of the best examples from these FLD measurements. Based purely on the mathematics and correspondence of the Merklein et al. (Ref 15) and Hotz et al. (Ref 8) correlation coefficients, we could easily and unequivocally identify the image corresponding to the time-history-dependent limit strain. As is well known, a sheet sample deforming in positive biaxial tension cannot theoretically develop a line of zero extension, which in turn becomes a flow instability. It is for this reason that Marciniak and Kuczynski (Ref 13) proposed that a sheet must contain an initial linear imperfection for the local neck to develop. Figure 8 shows the full-field Eulerian strains present in a balanced-biaxial tension specimen immediately before fracture.

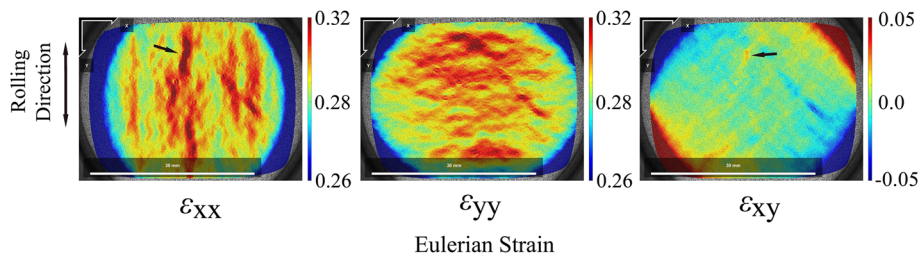


**Fig. 8** Eulerian strain fields for a balanced-biaxial MK experiment immediately before fracture

Rather than a single line of zero extension, individual ellipses of high deformation are seen in both principal strains,  $\epsilon_{xx}$  and  $\epsilon_{yy}$ . These zones are nearly aligned in several bands in the sheet rolling direction. While the contrast in the strain fields is dramatic, the difference in values is only between Eulerian strains of 0.28 and 0.32. The scales are equivalent for both principal strain fields. The shear strains,  $\epsilon_{xy}$ , are also shown in Fig. 8. They are nearly zero over the entire deforming section of the MK sample, indicating that this is a valid balanced-biaxial tension experiment. A point of slightly higher shear appears in the deforming test section, marked with an arrow. This sample point is also indicated in the  $\epsilon_{xx}$  principal strain-field plot. Fracture initiated at this point a second later.

Although there was not a single line of zero extension deformation that developed in the sample shown in Fig. 8, the strain-acceleration curves were smooth. They appeared as shown in Fig. 7, and it was straight forward to adjust the data smoothing to obtain a correspondence between the Merklein et al. (Ref 15) and Hotz et al. (Ref 8) techniques.

#### 4.4 Forming-Limit Curves

The MK forming experiments covered the complete strain range between uniaxial tension and balanced-biaxial tension, and multiple experiments were performed along each particular strain path. The results are plotted in Fig. 9 as true (logarithmic) principal strains and points from both the Bragard type, ISO 12004-2:2008 (Ref 9) and temporal analyses are shown. Each individual pair of points, Bragard and temporal, corresponds to a separate experiment, and each symbol's shape indicates a different specimen geometry or width.

These loci of forming-limit data have the classic shape, with a minimum at or just to the right of plane strain and maximums in uniaxial and balanced-biaxial tension. There is a minimum amount of experimental dispersion for both the Bragard and temporal analyses in-plane strain and on the left-hand side of the forming-limit diagram. However, experiment dispersion is significant as one traverses from plane strain toward and including balanced-biaxial tension. This dispersion is more pronounced for the temporal analysis.

As would be expected, the results from the temporal analysis lie above those calculated using the analysis of ISO 12004-2:2008 (Ref 9). The Bragard-type criterion takes data outside of the instability, while the temporal analysis averages data within the plastic instability. In balanced-biaxial tension, results from the two techniques are nearly identical and with the experimental dispersion partially overlap. Moving from a balanced-biaxial state to plane strain the results from the two techniques began to diverge. In plane strain, the difference is about 40%. This significant amount of spread continues through to uniaxial tension.

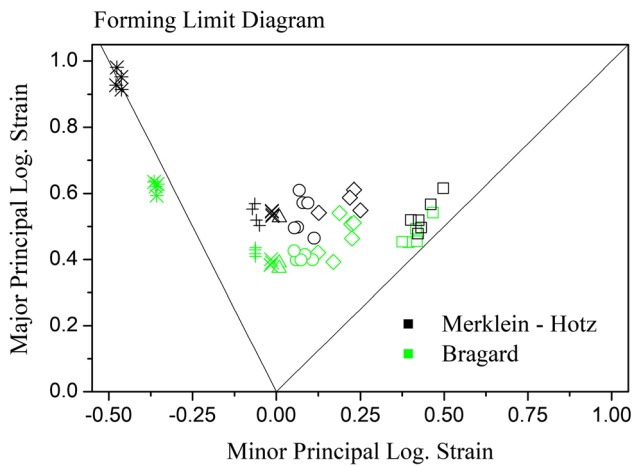


**Fig. 9** The true (logarithmic) limit strains for the cold-rolled steel used in this study. Results from both the Bragard type and temporal analyses are shown

## 5. Discussion

Two FLDs, inside and outside of the necking instability, for cold-rolled steel sheet were obtained using the Bragard-type analysis and the proposed correspondence of the correlation coefficient techniques. We believe these results can be viewed with confidence. The MK sample has minimal strain gradients over its deformation zone, facilitating the Bragard-type analysis and making it relatively insensitive to the boundaries set for fitting the inverse polynomial. The temporal analysis is purely mathematical and requires minimal interpretation. Our smoothing analysis recognizes that experimental noise is a key feature in digital-image correlation strain data, but we take advantage of it to obtain a unique value for a temporal-based limit strain.

Our FLD results show that there is validity in considering both the Bragard and temporal analyses. These very different approaches, one based on strains outside of the necking instability and the other strains inside, produce overlapping results in biaxial tension but divergent limit strains in plane strain and uniaxial tension. Depending on the application and criticality of confidence in the forming operation, engineers could consider data from the two approaches as upper and lower forming-limit bounds. They could then design a forming operation accordingly.

The full-field strain measurements showed that a line of zero extension or MK defect never developed in balanced-biaxial tension. Correspondingly, there was very little difference between limit strains based on deformations inside and outside of the instability. The absence of such a MK defect appears to have limited the material's ability to postpone failure by shifting deformation outside of the developing neck. Once a diffuse instability occurred the material quickly failed. On the other hand, when a line of zero extension did form, in plane strain and uniaxial tension, the material had the ability to resist necking failure as discussed by Ghosh (Ref 7). We measured a forming limit within the necking instability that was 40% higher than that from the Bragard analysis. Thus, the Bragard analysis appears to be excessively conservative in these deformation states.

It should be noted that neither Merklein et al. (Ref 15) nor Hotz et al. (Ref 8) showed as great a difference between the

Bragard profile method and their time-dependent analyses. This could be attributed to several factors. This is possibly a result of a difference in the material for which the data are shown. Our cold-rolled steel was moderately strain rate sensitive, which, as noted, will push the deformation away from the instability into the bulk of the specimen and delay formation of an acute necking instability. Merklein et al. and Hotz et al. also used a Nakazima punch and die configuration. This geometry exhibits steeper strain gradients than the MK sample geometry, which is practically gradient free. The steep strain gradient could raise the results of the Bragard fit and draw it closer to the results of the time-dependent analysis.

There are other important observations that arise from our theoretical analysis. It was performed using ideal functions and demonstrated that Merklein et al.'s (Ref 15) technique is extremely dependent on experimental noise. Without it, the analysis never exhibits the peak in correlation coefficient that the authors use to define the initiation of the necking instability and thus limit strain. With the addition of noise to the functions, the peak seen experimentally appears, but we also found that the time/image number at which it occurs depends on the extent of the noise present. These results indicate that taken alone the full correlation coefficient analysis would not be the most reliable determinate of the forming-limit strain.

Hotz et al.'s (Ref 8) gliding correlation coefficient seeks the maximum curvature in the strain-acceleration curve, and this curvature appears to be largely independent of noise when studied with the ideal functions. Although, if there is excessive noise in the experimental strain/time data, many deep valleys occur in the gliding correlation coefficient/time curve. This can make it difficult to resolve which valley corresponds to the maximum curvature.

Thus, for the Merklein/Hotz techniques, experimental noise is a double-edged sword. It is both necessary for the analyses but also produces uncertainties in the results, which indicates that our smoothing technique has benefits. Our experiments on a cold-rolled steel very closely mimic the results obtained with the ideal functions and superimposed Gaussian noise, lending confidence to the experimental technique and analysis. By varying the smoothing of the strain/time (image number) data, we were able to identify the valley in the gliding correlation coefficient due to the maximum in curvature in the strain-acceleration curve and obtain a correspondence to the full correlation coefficient. It is worth noting that contrary to the result for the ideal functions in the actual experiments the limit-strain result from Hotz et al.'s (Ref 8) analysis showed a slight sensitivity to the amount of smoothing. This makes obtaining a correspondence between the two techniques for determining a limit strain necessary.

## 6. Conclusions

We developed a modified Merklein/Hotz analysis and used it to obtain a complete forming-limit diagram for a cold-rolled steel. This is an FLD made possible by the digital-image correlation technique and is based solely on deformation in the zone that will become the necking instability. This temporal FLD stands in contrast to the standard FLD based on the 2008 norm, which relies on deformations measured outside of the necking instability. From the differences in these two FLDs we came to the following conclusions:

1. Engineers should consider loci of limit data from both a Bragard-type analysis, as discussed in the norm ISO 12004-2:2008 (Ref 9) and a temporal approach that relies on strains within the necking instability. For our cold-rolled steel sheet and our temporal analysis, the Bragard technique appears to be excessively conservative in plane strain and uniaxial tension, by as much as 40%.
2. Merklein et al.'s (Ref 15) computational, correlation coefficient technique requires that experimental noise is present in the strain versus time/image number data. However, at the same time, the image number, "limit strain," where Merklein et al.'s (Ref 15) correlation coefficient peak occurs depends on the amount of experimental noise present.
3. When applying Hotz et al.'s (Ref 8) gliding correlation coefficient analysis, it can be difficult to identify the *gliding correlation-coefficient* valley associated with the maximum curvature in the acceleration data. In this case, it is necessary to compare results based on multiple sets of analyses using various parameters.
4. A correspondence between Merklein et al. (Ref 15) and Hotz et al. (Ref 8) techniques defines a unique image and thus limit strain, as the two techniques are independent and utilize different properties in the acceleration/time (image number) curve. Thus, this approach is consistent for multiple experiments over a variety of strain paths and determines a reliable FLD with minimal experimental scatter.

## Acknowledgments

The authors are grateful for the financial support provided by ANPCyT PICT-A 2017-2970. We also wish to thank Martin Leonard for the optical metallography and the software used in the uniaxial tension and Bragard-type analysis. We also acknowledge the invaluable support of Fernando Ugo in performing the forming-limit and tension experiments.

## Appendix—Part I Constants

A graphic representation of the two functions, Eq 2 and 3, with which we fitted the plane-strain experimental strain image/time curve is shown in Fig. 10. The experimental data were taken from a Marciniak and Kuczynski limit-strain experiment following a plane-strain deformation path. An image/time of 140 is the final point of the double-exponential function and the beginning of the third-power polynomial. The slopes of these two functions, in strain, strain rate and strain acceleration versus time (image number) were set equal at point 140 making the splice between the functions seamless.

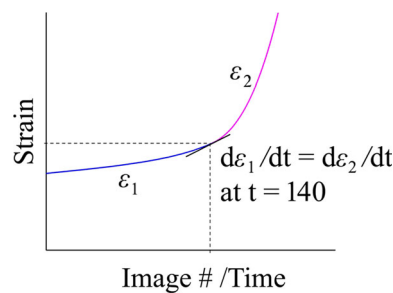


**Fig. 10** A graphical representation of the two functions used to fit the experimental strain vs. image/time curve

Values of the coefficients in Eq 2 and 3 are given in Table 2.

## Appendix—Part II Strain Radius

For our measurement of limit strains, we used a strain radius of five points in the Ncorr calculation. This number of points was sufficient to minimize the noise that can result from the differentiation of displacements, but it was necessary to verify that we were not reducing the fidelity of the strain calculation by using too many points. To this end, we repeated our analysis of a plane-strain sample using a strain radius of three and two, as well. Figure 11 shows the region of the sample studied with Ncorr, which contains the line of zero extension, plastic-necking instability. A sample point appears in the center of the region of interest, as well as the accompanying points from which the strains were calculated. For strain radii of five, three and two, 81, 29 and 13 points, respectively, were used in the strain calculation.

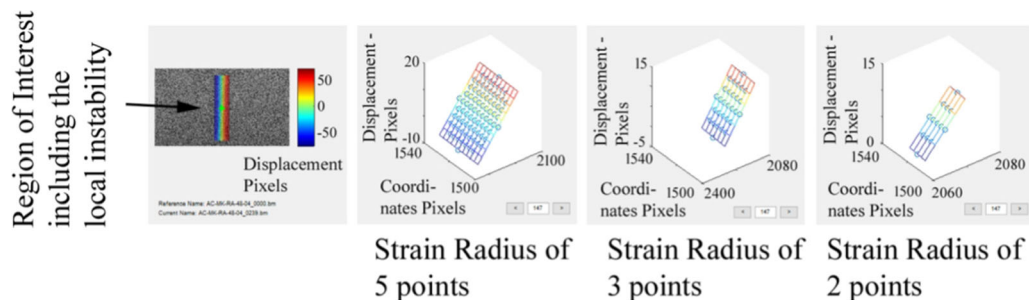
Figure 12 is a plot of the  $\epsilon_{xx}$  Lagrangian strain field calculated using a strain radius of five. The plastic instability, line of zero extension, is clearly visible in the center of the region of interest. The sample point shown in Fig. 11 is seen to lie within the instability, and the points associated with the different strain radii appear to successfully capture the gradients associated with the instability.

Figure 13 shows the results of the Merklein et al. (Ref 15) and Hotz et al. (Ref 8) calculations for the different strain-radii Ncorr calculations. We used a polynomial smoothing of five points and a gliding Hotz et al. band of seven points, for all cases. It can be seen that with the exception of very slight variations in the noise profile shown by the gliding analysis the results are equivalent, irrespective of the strain radius. In all cases, we found a correspondence between the two techniques at equivalent points in time, image number. The limit strains that resulted from the calculations are tabulated in Table 3. The results are for practical purposes the same. There was no loss in



**Table 2 Strain versus time (image number) fitting parameters**

$\varepsilon_1 _{t=1 \text{ to } 150} = \varepsilon_0 + A_1 e^{\frac{(t-t_0)}{c_1}} + A_2 e^{\frac{(t-t_0)}{c_2}}$	$\varepsilon_2 _{t=140 \text{ to } 150} = a(t-140)^3 + b(t-140)^2 + c(t-140) + \varepsilon_1 _{t=140}$
$t = 1 \text{ to } 140$	$t = 140 \text{ to } 150$
$\varepsilon_0 = 0.01993$	$\frac{d^3 \varepsilon_1}{dt^3} _{t=140} = 6a = 6.9405 \times 10^{-4}$
$t_0 = 78.45089$	$\frac{d^2 \varepsilon_1}{dt^2} _{t=140} = 2b = 0.0035$
$A_1 = 3.03033 \times 10^{-7}$	$\frac{d\varepsilon_1}{dt} _{t=140} = c = 0.022$
$A_2 = 0.28457$	$\varepsilon_1 _{t=140} = 0.6286$
$c_1 = 4.91821$	
$c_2 = 100.12609$	
Reduced $\chi^2 = 4.97 \times 10^{-5}$	



**Fig. 11** The region of interest, a sample point at which the strains will be calculated, and the points to be used in the strain calculation are shown for strain radii of five, three and two points

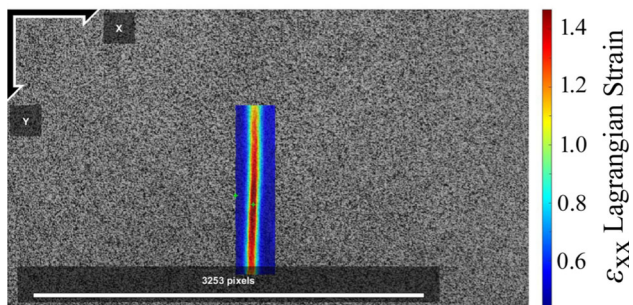


**Fig. 12** The  $\varepsilon_{xx}$  Lagrangian strain field associated with the region of interest and displacements shown in Fig. 11, for the plane-strain specimen. The calculation was performed for a strain radius of five points

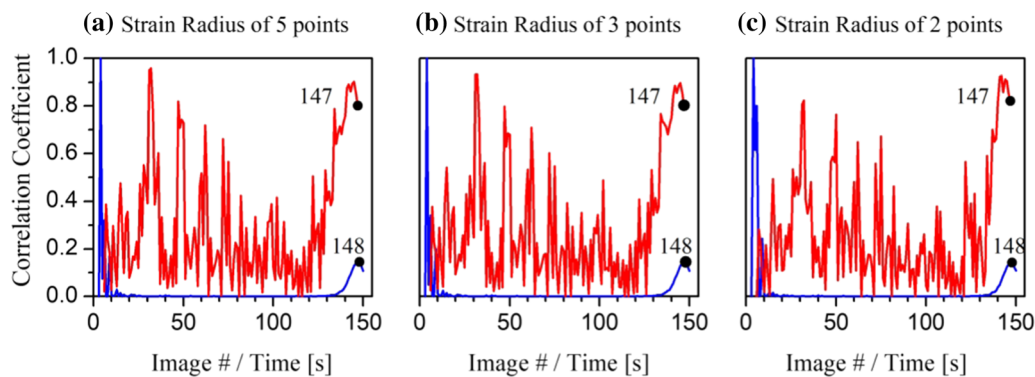


**Fig. 13** Results from the Merklein et al. (Ref 15) and Hotz et al. (Ref 8) correlation coefficient techniques applied to a plane-strain MK sample for different strain radii in the Ncorr digital-image correlation analysis. (a) Strain radius of five points, (b) three points and (c) two points

**Table 3 Parameters used in the digital-image correlation analysis and the resulting temporal analysis**

Ncorr strain radii					
Five		Three		Two	
Major log. limit Strain	Minor log. limit Strain	Major log. limit Strain	Minor log. limit Strain	Major log. limit Strain	Minor log. limit Strain
0.5272	0.0092	0.5277	0.0091	0.5280	0.0113

Plane-strain MK sample, Ncorr parameters: subset radius = 50; subset spacing = 2; diff. norm cutoff =  $10^{-6}$ ; number of iterations cutoff = 50  
Also listed are the calculated, logarithmic limit strains

fidelity when calculating the strains with a strain radius of five and 81 points in total.

## References

- J. Blaber, B. Adair, and A. Antoniou, Ncorr: Open-Source 2D Digital Image Correlation Matlab Software, *Exp. Mech.*, 2015, **55**, p 1105–1122
- A. Bragard, J.C. Baret, and H. Bonnarens, A Simplified Technique to Determine the FLD at the Onset of Necking, *Rapp. Centre Rech. Metall.*, 1972, **33**, p 53–63
- M. Gensamer, Strength and Ductility, *Trans. Am. Soc. Met.*, 1946, **36**, p 30–60
- G.M. Goodwin, Application of Strain Analysis to Sheet Metal Forming Problems in the Press Shop, *SAE Technical Paper*, No. 680093 (1968), pp. 380–387
- GOM, *GOM Service Area* [Online] (GOM, 2019). Available: <http://www.gom.com/metrology-systems/aramis.html>. Accessed 20 Dec 2019
- A.K. Ghosh and S. Hecker, Failure in Thin Sheets Stretched Over Rigid Punches, *Metall. Mater. Trans. A*, 1975, **6A**, p 1065–1074
- A.K. Ghosh, The Influence of Strain Hardening and Strain-Rate Sensitivity on Sheet Metal Forming, *Trans. ASME J. Eng. Mater. Technol.*, 1977, **99**(3), p 264–274
- W. Hotz, M. Merklein, A. Kuppert, H. Friebe, and M. Klein, Time Dependent FLC Determination: Comparison of Different Algorithms to Detect the Onset of Unstable Necking Before Fracture, *Key Eng. Mater.*, 2013, **549**, p 397–404
- International Standard ISO 12004-2:2008, *Metallic Materials—Sheet and Strip: Determination of Forming-Limit Curves. Part 2—Determination of Forming-Limit Curves in the Laboratory*, International Organization for Standardization, Geneva, 2008
- R.A. Iquilio, F.M. Castro Cerda, A. Monsalve, C.F. Guzmán, S.J. Yanez, J.C. Pina, F. Vercruyse, R.H. Petrov, and E.I. Saavedra, Novel Experimental Method to Determine the Limit Strain by Means of Thickness Variation, *Int. J. Mech. Sci.*, 2019, **153-154**, p 208–218
- S.P. Keeler and W.A. Backofen, Plastic Instability and Fracture in Sheets Stretched Over Rigid Punches, *Trans. Am. Soc. Met.*, 1963, **56**, p 25–48
- M.E. Leonard, F. Ugo, M. Stout, and J.W. Signorelli, A Miniaturized Device for the Measurement of Sheet Metal Formability Using Digital Image Correlation, *Rev. Sci. Instrum.*, 2018, **085114**, p 89–95
- Z. Marciniak and K. Kuczynski, Limit Strains in the Processes of Stretch-Forming Sheet Metal, *Int. J. Mech. Sci.*, 1967, **9**, p 609–620
- A.J. Martínez-Donaire, F.J. García-Lomas, and C. Vallengano, New Approaches to Detect the Onset of Localised Necking in Sheets under through-Thickness Strain Gradients, *Mater. Des.*, 2014, **57**, p 135–145
- M. Merklein, A. Kuppert, and M. Geiger, Time Dependent Determination of Forming Limit Diagrams, *CIRP Ann. Manuf. Technol.*, 2010, **59**, p 295–298
- J. Min, T.B. Stoughton, J.E. Carsley, and J. Lin, Comparison of DIC Methods of Determining Forming Limit Strains, in *International Conference on Sustainable Materials Processing and Manufacturing, SMPM 2017. Procedia Manufacturing*, vol. 7 (2017), pp. 668–674
- K. Nakazima, T. Kikuma, and K. Hasuka, Study on the Formability of Steel Sheets, *Yawata Technical Report*, No. 264, (1968), pp. 8517–8530
- M.A. Sutton, J.-J. Orteu, and H.W. Schreier, *Image Correlation for Shape, Motion and Deformation Measurements*, Springer, New York, 2009
- P. Vacher, A. Haddad, and R. Arrieux, Determination of the Forming Limit Diagrams Using Image Analysis by the Correlation Method, *CIRP Ann. Manuf. Technol.*, 1999, **48**, p 227–230
- W. Volk and P. Hora, New Algorithm for a Robust User-Independent Evaluation of Beginning Instability for the Experimental FLC Determination, *Int. J. Mater. Form.*, 2010, **4**, p 1–8
- K. Wang, J.E. Carsley, B. He, J. Li, and L. Zhang, Measuring Forming Limit Strains with Digital Image Correlation Analysis, *J. Mater. Process. Technol.*, 2014, **214**, p 1120–1130

**Publisher's Note** Springer Nature remains neutral with regard to jurisdictional claims in published maps and institutional affiliations.